Environmental Science Processes & Impacts

ROYAL SOCIETY OF CHEMISTRY

PAPER

View Article Online
View Journal | View Issue

Cite this: *Environ. Sci.: Processes Impacts*, 2025, **27**, 2394

Arbuscular mycorrhizal fungi influence the speciation and subcellular abundance of uranium in plant roots†

James M. Dinsley, *[ab] Kirstie Halsey, [c] Eudri Venter,[cd] Miguel A. Gomez-Gonzalez, [e] Katie L. Moore, [f] Lorraine P. Field, [g] Samuel Shaw, [a] Clare H. Robinson[a] and Jon K. Pittman *[a]

Uranium (U) is a natural radioactive metal and a persistent environmental pollutant. Characterising the influence of arbuscular mycorrhizal fungi (AMF) on U bioaccumulation and partitioning in plants is crucial to understand U soil-to-plant transfer mechanisms. High resolution elemental mapping, spectroscopy and microscopy techniques were conducted on uranyl nitrate dosed *Plantago lanceolata* roots colonised with *Rhizophagus irregularis*. U-rich particles accumulated within the root cells, with higher abundance in epidermal and outer cortex cells of mycorrhizal root samples than in non-mycorrhizal roots. Electron microscopy determined two different crystalline U phases, an acicular crystal and a novel rounded aggregate formation, the latter of which was only found within the mycorrhizal root cells. Multiple imaging and spectroscopic techniques enabled the dominant elements with these U biominerals to be determined. Co-localisation between U, phosphorus and oxygen indicated the dominance of U-phosphate biominerals, but metals including calcium and zinc were also found to co-localise. The most dominant U compound was uranyl orthophosphate, likely accompanied by autunite. This study demonstrates alteration in U localisation and U particle morphology within *Plantago* roots as a direct consequence of AMF colonisation. This knowledge will allow more accurate U food-chain transfer modelling and better assessment of AMF-assisted phytoremediation feasibility.

Received 10th February 2025
Accepted 13th June 2025

DOI: 10.1039/d5em00108k

rsc.li/espi

Environmental significance

The environmental contamination of toxic radionuclides such as uranium is of concern because of the damaging consequences to individual organisms and ecosystems. The accumulation of uranium into plants and fungi provides a route for wider transfer into higher levels of a food chain but also provides possibility for use of these organisms for bioremediation. Detailed chemical characterisation of uranium within plant root and fungal tissues allows determination of the stability and potential mobilisation of the uranium into above-ground tissues. Furthermore, it is important to understand the influence of mycorrhizal fungal association in controlling the amount and form of uranium accumulation in plant roots. This will determine how important a fungal contribution is to viable plant bioremediation strategies.

Introduction

Uranium (U) occurs naturally in multiple oxidation states, including U(IV) and U(VI), and as various radioisotopes, with ^{238}U being the most abundant and one of the most persistent (half-life of 4.468×10^9 years).[1] U-rich ores are critical to the nuclear fuel cycle, and so are mined, milled and fabricated into materials for nuclear power plants, which play an important role in a decarbonised energy sector.[2] Overall, a variety of these nuclear fuel cycle processes have led to the release of U into the environment. This includes long-lasting radioactive topsoil U contamination that can accumulate *via* plants into the wider environment and is challenging to remediate; for example, the U contamination at the South Terras mine site in Cornwall, UK[3] or at the Sevilha mine in Beiras, Portugal.[4] Better understanding

[a]*Department of Earth and Environmental Sciences, Faculty of Science and Engineering, The University of Manchester, Manchester, UK. E-mail: jon.pittman@manchester.ac.uk*

[b]*Waste and Residue Processing, United Kingdom National Nuclear Laboratory, Springfields, Salwick, Preston, UK. E-mail: james.dinsley@uknnl.com*

[c]*Bioimaging Facility, Department of Computational and Analytical Sciences, Rothamsted Research, Harpenden, UK*

[d]*JEOL UK, Watchmead, Welwyn Garden City, UK*

[e]*Diamond Light Source, Harwell Science and Innovation Campus, Didcot, UK*

[f]*Photon Science Institute, Department of Materials, Faculty of Science and Engineering, The University of Manchester, Manchester, UK*

[g]*Decarbonisation and Resource Management, British Geological Survey, Keyworth, Nottingham, UK*

† Electronic supplementary information (ESI) available. See DOI: https://doi.org/10.1039/d5em00108k

of U uptake and accumulation into plants is needed to determine whether phytoremediation of U-contaminated soils is feasible, and to accurately model how U might impact ecosystem health through trophic level transfer. Whilst advances have been made to understand the geochemical behaviour of U within soils,[5–7] much less is known about U dynamics within plant tissues. Knowledge gaps also exist regarding the role of soil microbiota, such as arbuscular mycorrhizal fungi (AMF), on influencing soil-to-plant U transfer.[8,9]

Many prior studies exploring U uptake from soil to plants have focussed on the simple determination of total U content within different compartments of the plant,[10–12] or the comparison of soil-to-root or root-to-shoot transfer factors.[4,13,14] Alternatively, many studies have examined the feasibility of a specific plant species to act as an accumulator to accelerate the decontamination of contaminated sites.[4,15] These studies provide a solid background understanding to the various geochemical and biological conditions that may affect soil to plant transfer of U. However, investigations rarely consider the contribution of AMF to plant U bioaccumulation or may rely on the study of model plants that are typically non-mycorrhizal (*e.g.*, *Arabidopsis thaliana*).[16,17] AMF are obligate symbionts with many land plants, which typically allow the transfer of essential micronutrients to the plant hosts in exchange for photosynthetically produced carbon, but sometimes also non-essential toxic metals can be transferred.[18,19] Those studies that have examined the consequence of AMF colonisation have typically only focussed on bulk U accumulation in whole plant and fungal tissues, without consideration of cell-to-cell differences in U accumulation and with little investigation into the U speciation or mechanisms of accumulation.[3,9,20,21]

As electron and X-ray microscopy and elemental mapping techniques have advanced in resolution and accessibility,[22] the ability to visualise the distribution and speciation of U within plants has improved.[23] For example, U localisation has been shown to correlate with phosphorus (P) distribution within the roots of various plant species, indicating that enhanced P content results in the precipitation and immobilisation of U within root cells.[23,24] Prior literature studies have examined the morphology of U within plant tissues and discovered the presence of U-rich acicular needle minerals precipitated along the cell walls and cytoplasm of the root cells.[25] Synchrotron X-ray absorption spectroscopy (XAS) has also determined the U speciation within roots, such as for *Helianthus annuus* and *Brassica napus,* in which U is mostly present as an undetermined uranyl phosphate biomineral.[25] However, neither subcellular characterisation of U localisation nor U chemical speciation assessment has so far been examined in roots as a direct response to the presence of AMF. This is most likely owing to challenges with visualising both the intracellular AMF structures and the U localisation simultaneously. Furthermore, while prior work has examined the likely U biomineralisation pathways for free-living fungi and *ectomycorrhiza*, the intrinsic nature of AMF means that the biomineralisation behaviour of U within intracellular hyphae is seldom studied and poorly understood.[26,27]

This study aimed to characterise U behaviour within roots of uranyl(VI) dosed *Plantago lanceolata*, colonised with the AMF species *Rhizophagus irregularis*, by using a combination of electron microscopy, nanoscale secondary ion mass spectrometry (NanoSIMS) and synchrotron radiation (SR) X-ray techniques, to uncover a deeper understanding of how AMF influences root uptake and storage of U. Plants were grown in a nutrient-containing sand substrate rather than natural soil, to reduce soil particle adherence to roots that can hinder reliable nanoscale elemental imaging of root sections. *P. lanceolata* was selected as the host plant species for this investigation owing to its relatively fast growth rate and extensive use in AMF colonisation experiments, while *R. irregularis* has also been frequently used as a model AMF species, has been detected in U contaminated environments, and has been shown to enhance U content in plant tissues.[3,8,21,28] It was hypothesised that AMF colonisation would result in enhanced U uptake owing to the acquisition of U through both direct root uptake and AMF extracellular hyphae extraction, with this U being stored *in planta* as needle-like, U-phosphate crystals, in line with prior findings. This investigation provides a novel insight into the direct influence of AMF colonisation on the uptake, localisation and speciation of U within plant roots. This is critical knowledge for advancing current understanding of U biomineralisation. This is challenging owing to the difficulty in establishing whether U uptake or storage behaviours exhibited by plant-fungal symbiosis are plant-driven or AMF-driven. However, by directly assessing the contribution of AMF to U sequestration in plants, the ability to better model U migration within an ecosystem or establish effective bioremediation strategies for U-contaminated land can be improved.

Methods

Plant materials, AMF inoculation and U dosing

For the experimental design, four treatments were compared: (1) plants with no U addition and no AMF inoculation; (2) U-dosed plants with no AMF inoculation; (3) AMF inoculated plants with no U addition; (4) AMF inoculated and U-dosed plants. A minimum of 20 plant pots were sown to allow at least five replicates for each of the four treatments. *P. lanceolata* seeds (Emorsgate Seeds) were surface sterilised in 30% (v/v) sodium hypochlorite solution then rinsed five times in sterile deionised water. Sterilised seeds were transferred (30 seeds per pot) to pre-sterilised plastic pots (8 cm top diameter × 7.5 cm bottom diameter × 8 cm height) containing 450 g of horticultural grade, acid-washed and autoclaved sand. The bottom of each pot was lined with a sterilised 35 μm mesh to prevent the loss of small sand grains. A 100 ml volume of sterile Hoagland's No. 2 basal salt mixture nutrient solution (Sigma-Aldrich) was added to each pot. Pots were stored within sun bags (Sigma-Aldrich) that block microbial entry, reduce water loss and enable gas exchange through a micropore filter (0.02 μm) on the face of the bag. *R. irregularis* spores (Symplanta) were prepared as an inoculant in 1.5 g of Fuller's earth clay mineral powder (Sigma-Aldrich) per plant pot (approximately 6000 spores), which was mixed with water and passed through a 38 μm sieve

and the resulting spore solution applied to the sand substrate in the pots of the inoculation treatments. The spore solution was added immediately following the addition of *P. lanceolata* seeds and the nutrient solution. A U spike solution was made using $UO_2(NO_3)_2$ solid particles and deionised water to give 350 ppm of U, which was adjusted to pH 4 to maximise UO_2^{2+} formation. Aliquots of 100 ml were used to dose each pot giving a total available U per pot of 35 mg (78 mg kg^{-1} of sand). U dosing took place 3 weeks after the initial seeding of the pots to enable sufficient preliminary plant growth and minimise adverse toxicity effects.

Plant preparation

Plants were incubated in a Panasonic environmental chamber (MLR-352-PE Series) for 12 weeks, under a 16 h light at 22 °C, and 8 h dark at 15 °C cycle, with a photon flux density of 40 μmol m^2 s^{-1}. Pots were systematically rotated by one position each week to prevent differences in chamber light access from being a limiting growth factor. After 12 weeks, individual *P. lanceolata* plants were extracted from the sand and washed with deionised water. Whilst biomass is a common indicator for plant growth, shoot and root length was used instead to enable individual plant specimens to be reliably and more precisely measured due to low biomass amounts per plant. Shoots and roots were separated and photographed to quantify mean shoot and root length using ImageJ (Fiji v. 2.3.0). Approximately 10% of the roots from each sample were preserved in 70% (v/v) ethanol solution for aniline blue staining to determine AMF colonisation, as described by Davies *et al.*[8] and Rosas-Moreno *et al.*[9] Some of the shoot and root material from each treatment was transferred into 1.5 ml cryovials and stored anaerobically at −80 °C in preparation for bulk synchrotron XAS. Other washed root samples underwent high pressure freezing, resin embedding and thin sectioning for subsequent scanning electron microscopy (SEM) or scanning transmission electron microscopy (STEM) with energy dispersive X-ray spectroscopy (EDS), SR microscale X-ray fluorescence (SR μ-XRF), NanoSIMS, and optical microscopy or transmission electron microscopy (TEM). Residual root and shoot material was dried at 40 °C overnight in a drying oven for acid digestion and multi-elemental quantification of U, P, potassium (K), sulphur (S), calcium (Ca), copper (Cu) and zinc (Zn) by inductively coupled plasma mass spectrometry (ICP-MS), exactly as described by Rosas-Moreno *et al.*[9]

Section preparation

Cleaned root samples were infiltrated with 0.5 M MES buffer (pH 5.4), and were high pressure frozen in 6 mm sample carriers using a Leica HPM 100 high pressure freezer (Leica Microsystems). High pressure freezing was the chosen sample preparation method as NanoSIMS does not allow for analysis of hydrated samples. While some elemental redistribution is unavoidable during dehydration and resin embedding, high pressure freezing, dehydration and resin embedding is widely considered to be the best available sample preparation route for NanoSIMS to minimise sample preparation artefacts.[29] Samples were transferred to 100% (v/v) ethanol in liquid N_2 and placed in a Leica EM AFS automatic freeze substitution system (Leica Microsystems). Whilst uranyl acetate is a commonly used biological stain, osmium tetroxide (OsO_4) was used instead to prevent interference with *in situ* U. Samples were sequentially warmed to −30 °C over 5 days, then to 4 °C over 2 days, and finally brought to room temperature. The samples were processed through increasing concentrations of LR White resin (Agar Scientific) and embedded at 58 °C for 16–20 h in a N_2 rich environment. The resin blocks were cut with a Leica RM2265 rotary microtome to prepare semi-thin sections for SEM-EDS (10 μm), SR μ-XRF (10 μm), NanoSIMS (1 μm) and dye-stained microscopy (10 μm). The sections were dried onto aluminium (Al) stubs (for SEM-EDS), silicon (Si) wafers (for NanoSIMS), or Si nitride windows (for SR μ-XRF). Sections for optical microscopy were dried onto polysine slides at 60 °C, before applying a drop of aniline blue dye stain to the section for 30 s, then the excess dye was washed off and the section dried again. Resin blocks were cut into ultra-thin sections (100 nm) using a Leica UC7 ultramicrotome and a DiATOME diamond knife, and mounted onto 3 mm^2 Pioloform coated Cu grids (Agar Scientific) for TEM and STEM-EDS.

SEM-EDS, STEM-EDS and TEM

The Al stubs with the root thin sections were coated with a thin film of carbon (25 μm) using a turbo carbon coater (Agar Scientific). Analysis was carried out using a Quanta 600 environmental SEM (FEI Company) fitted with a 2-element backscattered electron detector and connected to an INCA 450 energy dispersive X-ray microanalysis system (Oxford Instruments) with a 50 mm^2 Peltier-cooled silicon drift X-ray detector. The SEM was operated under high vacuum mode with a working distance of 10 mm, using an electron beam accelerating potential of 10–20 keV with electric currents of 0.2–1.2 nA. The distribution of elements within the sections was determined using quantitative energy-dispersive electron probe point microanalysis. Point spectra were obtained to confirm the identity of elements present within selected regions. Spectra were processed using the INCA Microanalysis Suite software (ver. 5.05, Oxford Instruments), with elemental maps produced from multiple framed scans (30–60 scans over 0.5–2 h) of an element. Maps were obtained at a resolution of 1024 × 1024 pixels and used a 20 keV electron beam with an approximately 0.31 nA beam current in order to generate sufficient X-ray counts (~28 000 counts per s) to enable high-resolution elemental mapping of root cross sections. ImageJ was used to quantify U particle size and abundance within sections. TEM analysis for morphological characterisation was carried out on a JEOL JEM-2100Plus microscope operated at 200 keV. STEM-EDS for elemental mapping used an Oxford Instrument Standard Ultimax TEM with an 80 mm^2 windowless X-ray detector, with Oxford Aztec software, and generated elemental maps at 1024 × 1024 pixel resolution. TEM imaging was achieved using a Gatan OneView IS camera with the Gatan Microscopy Suite (GMS3) software (ver. 3.32.2403.0), and STEM imaging done with a conventional darkfield (DF) STEM detector fitted to the

JEM-2100Plus (JEOL). False colour images were generated for each elemental map to show the intensity of each element detected within root cross sections. Regions of interest (ROIs) were selected to span each of the main important plant root layers (epidermis, cortex, endodermis and stele) from multiple separate zones across different replicate root sections in order to gain a representative perspective of elemental localisation and particle morphology differences. Thin section regions with physical damage (*e.g.*, folds, microfissures) or artefacts (*e.g.*, sand grains) were dismissed from the analysis. An ROI strategy was essential as it was not practicable to examine the entirety of each thin section at a high magnification. The TEM images of root sections from AMF-colonised plants were compared with TEM images from published literature to reliably identify and annotate fungal tissues based on fungal structure morphology within the cross sections.[30–32]

NanoSIMS

For NanoSIMS mapping, a NanoSIMS 50L (CAMECA) enabled the simultaneous measurement of seven sputtered ionic species ($^{23}Na^+$, $^{31}P^+$, $^{40}Ca^+$, $^{28}Si_2{}^+$, $^{63}Cu^+$, $^{68}Zn^+$ and $^{238}U^+$) across the surface of each root cross section specimen. A focussed 16 keV O^- primary ion source with a current of 20–25 pA was used to generate positive ions, which were detected *via* the use of a double focusing mass spectrometer. Standards of $CuSO_4$, $ZnSO_4$, $NH_4H_2PO_4$ and $UO_2(NO_3)_2$ were prepared on fresh Si wafers and used to align the NanoSIMS detectors to ensure the correct chemical species were detected with no mass interference. Each region of analysis was pre-sputtered with a fluence of 1×10^{17} O^- ions per cm. The D_0 and D_1 aperture had a diameter of 100 μm and 200 μm, respectively. The entrance slit was set to 50 μm width, and the aperture slit was not used to increase secondary ion intensity. For image acquisition, raster size was set to 50 μm × 50 μm for regular scans (512 pixels), or 20 μm × 20 μm for higher magnification scans of regions of interest (256 pixels). Dwell time for each scan was 5000 μs per pixel, with each scan consisting of approximately 50 planes (slices in depth). The OpenMIMS plugin was used with ImageJ to drift correct each scan (containing multiple planes), sum all individual scans to produce composite images, and produce colour merge images for visualising the relative localisation of Ca, P and U. The same ROI selection strategy was utilised between the electron microscopy techniques and NanoSIMS.

SR μ-XRF and XAS

SR μ-XRF of the root thin sections was performed using the Hard X-ray Nanoprobe at the Diamond Light Source I14 beamline.[33] The I14 beamline was selected owing to its ability to provide both high-resolution XRF for microscale elemental mapping across the root sections, alongside its ability to offer a microscale X-ray absorption near edge structure (μ-XANES) capability to examine U oxidation state over specific, identifiable nanoparticles. This beamline provides monochromatic X-rays that are tuneable within an energy range of between 5–23 keV, giving a beam size focused on the root samples of ~50 nm. Fluorescent X-rays were collected by a four-element Si drift detector (Rayspec) with a solid collection angle of 0.8 sr. Raster (continuous) scanning was used to generate elemental maps for each sample. Fluorescence μ-XANES maps at the U L_3 edge were produced in regions of interest for both the non-mycorrhizal and AMF-colonised roots containing discrete U-rich compounds, following a similar approach to Morrell *et al.*[34] For SR μ-XRF, plant structural boundaries could not be observed so ROIs focussed on the reliable capture of multiple, distinct U localised regions and the elemental co-localisations observed. Bulk XAS spectra to enable XANES and extended X-ray absorption fine structure (EXAFS) analysis were acquired using the B18 (Core XAS; 36-element Ge detector) and I20 (Versatile X-ray Absorption Spectroscopy; 64-element Ge detector) Diamond Light Source beamlines[35,36] at the U L_3 edge *via* a liquid N_2 cooled cryostat. These bulk XAS techniques provided higher resolution XANES data than the μ-XANES capability of I14, at the cost of only providing a XANES assessment of the full bulk root and shoot material. Furthermore, whilst the B18 beamline was faster and more effective for analysing higher U content samples (in this case, the roots), the I20 beamline had a greater sensitivity capable of conducting XANES and EXAFS on lower concentration shoot samples (approximately 10-fold lower U content). Root samples were analysed with the B18 beamline by collecting 15 to 35 scans, and shoot samples were analysed with the I20 beamline by collecting 3 to 5 scans. The first inflection point at the K edge of a yttrium (Y) foil (17 038 eV) was used to calibrate the peak energies of the sample spectra as described by Foster *et al.*[37]

XANES and EXAFS analysis

U reference standard spectra for uranyl orthophosphate, autunite and uraninite were used to inform the analysis of the measured plant XANES and EXAFS spectra. Data visualisation of XANES and EXAFS scans used the Athena package (Demeter ver. 0.9.26). The Y foil energy shift correction was applied and an average scan was generated from replicates for each sample. Each average scan was normalised and plotted in k^3 weighting to generate XANES, and EXAFS (k space) and Fourier transform (R space) plots. For I14 μ-XANES, individual scans were averaged, stacked, aligned, normalised and converted into a composite image by principal components analysis (PCA) in MANTiS software. For B18 and I20 EXAFS scans, spectral fitting was conducted in Artemis software (Demeter ver. 0.9.26). Peak positions at different atomic radial distances for the collected spectra were compared to the positions of known X-ray scattering paths for torbernite, *meta*-autunite, liebigite, chernikovite and uranyl orthophosphate. An EXAFS fit model was generated using IFEFFIT calculations and multiple fit parameters (R factors, Debye–Waller factors, ΔE_0 values) were used to assess the quality of the fit against the measured plant spectra (ESI Table S1†).

Statistical analysis

Statistical analyses were conducted using Minitab statistical software (ver. 21.1.1) to determine the statistical significance of the differences and relationships in the acquired empirical

data. Pearson's correlation analyses were conducted to examine significant relationships between different elements acquired following ICP-MS analysis of the shoot and root tissues. *T*-tests and two-way ANOVA tests were used in the comparison of length, elemental concentration and AMF colonisation data to identify significant differences in the overall mean values across multiple groups, with a Tukey post-hoc comparison test further used to assess the significance of mean differences between specific treatments. The significance threshold (p) was set to 0.05.

Results

Uranyl(VI) dosing increases root and shoot U content and inhibits root growth independent of AMF colonisation

Optical microscopy of aniline-blue dye-stained *P. lanceolata* roots demonstrated successful colonisation of the plants by *R. irregularis* (ESI Fig. S1A†). However, no significant difference was observed in the proportion of roots colonised by either mycorrhizal arbuscules or hyphae as a result of U dosing (ESI Fig. S1B†). Sand to plant U transfer was evident within the U-dosed *P. lanceolata* plants, which had significantly greater ($p < 0.001$) mean U concentrations within both the root and shoot tissues, relative to the control seedlings where only background U concentrations were detected (Fig. 1A). However, there was no significant difference in mean U concentration between non-mycorrhizal and AMF-colonised plants. In non-mycorrhizal and AMF-colonised seedlings, roots contained a greater mean concentration of U than shoots by approximately 12.6- and 16.8-fold, respectively. Of the total available U within the sand, the non-mycorrhizal and AMF-colonised plants absorbed 0.9% and 1.1% of the U into their tissues, respectively. No significant differences in shoot and root concentration for other elements including P, K, S, Ca, Cu and Zn were observed regardless of *R. irregularis* presence or U dosing (ESI Table S2†).

The presence of *R. irregularis* did not significantly influence the shoot or root length of control or U-dosed plants (Fig. 1B). Shoot length was not significantly affected by the addition of U to the plants, both for non-mycorrhizal and *R. irregularis* colonised treatments, but there was a significant reduction in mean root length following U exposure for both the mycorrhizal ($p = 0.003$) and non-mycorrhizal ($p < 0.001$) plants (Fig. 1B).

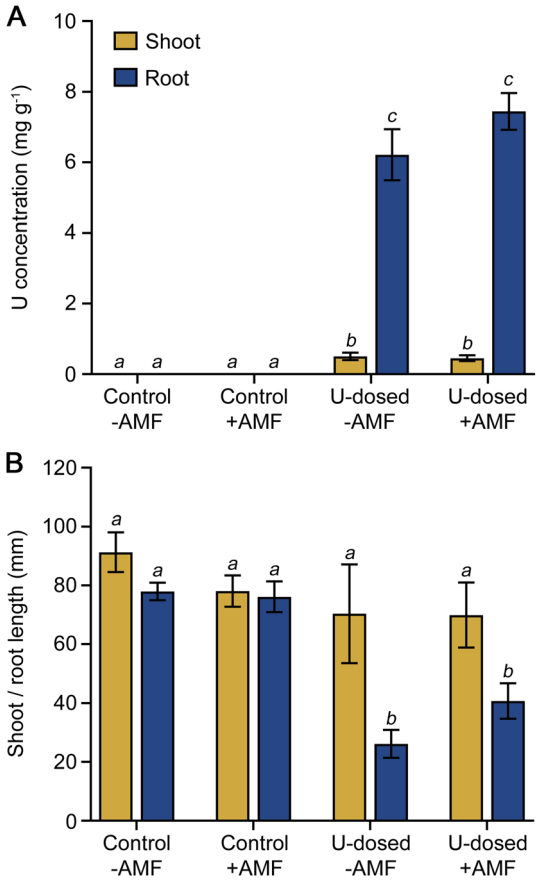

Fig. 1 U accumulation and plant growth response in control (un-dosed) and U-dosed non-mycorrhizal (−AMF) and mycorrhizal (+AMF) *P. lanceolata* seedlings. (A) Measurement of shoot and root U concentration. Control (background) U concentrations are all <0.0002 mg g^{-1}. (B) Measurement of shoot and root length. All data are mean values ± SEM, $n = 5$. Different lowercase letters indicate statistically significant differences ($P < 0.05$) between samples. This indicates that U dosing was successful and that this elevated U content is the likely cause for decreased mean root length. AMF had no significant influence on shoot and root U content or shoot and root length.

U-rich particles are larger and more abundant in AMF-colonised root cells

Examination of back-scattered electron (BSE) SEM images of *P. lanceolata* root thin sections found bright zones within the cells layers that were confirmed as U-rich regions by examination of EDS data, both in non-mycorrhizal (ESI Fig. S2†) and AMF-colonised (ESI Fig. S3†) samples. Within non-mycorrhizal plant specimens, U was rarely observed beyond the outermost epidermal layer, whilst U-rich particles were present within the inner cortex cells of the AMF-colonised specimens (ESI Fig. S4†). The distribution of these U-rich regions coincides with the location of fungal structures in the outer root cell layers.[38] There was a higher abundance of U-rich particles in specimens from AMF-colonised roots compared to those that were non-mycorrhizal, particularly within the outer root cell layers (epidermis and outer cortex), as quantified *via* ImageJ thresholding analysis of BSE images from SEM-EDS (Fig. 2A). In a representative comparison shown in Fig. 2, the total cumulative area of U-rich particles was 55.63 μm^2 in the non-mycorrhizal root cross section, whilst in the mycorrhizal root section U particles comprised a 5× larger total area of 278.23 μm^2. The mean size of the particles was significantly greater for the AMF-colonised roots compared to the non-colonised roots (Fig. 2B).

As expected, U-rich areas were not observed in any of the un-dosed control roots (ESI Fig. S5†). Not all bright regions in the BSE images correspond to U-rich areas, potentially representing other high atomic particles such as iron (Fe). For example, for one of the representative non-mycorrhizal root cells, two adjacent bright regions are shown to be differing compounds: one

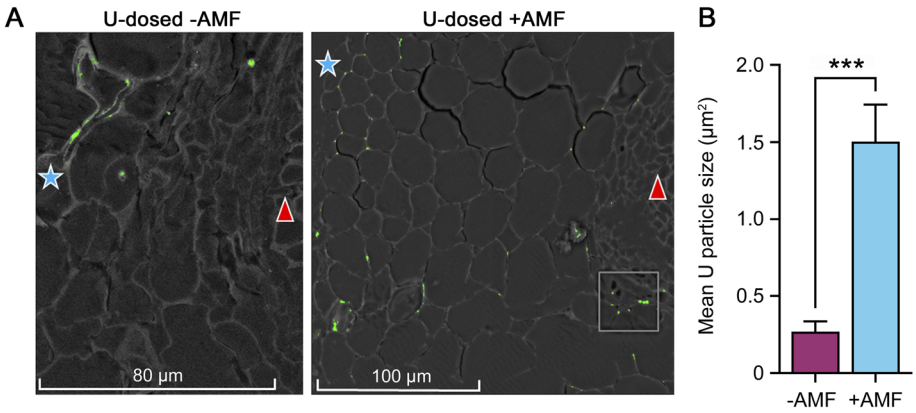

Fig. 2 Determination of U particle abundance. (A) BSE images spanning from the epidermis (blue star) through to the stele (red triangle) of a representative non-mycorrhizal (−AMF) and mycorrhizal (+AMF) root cross section. Bright, heavy atomic mass particles that exceed the ImageJ threshold of 0.13% are highlighted in green, depicting the location of U-rich particles across the entire root sections. The boxed region in the +AMF section was analysed in more detail, shown in Fig. 3A. (B) Quantification of particle size values in non-mycorrhizal (−AMF) and mycorrhizal (+AMF) root sections. Data are mean values ± SEM, $n = 208$ (−AMF) and $n = 185$ (+AMF). Asterisks indicate statistically significant differences ($p < 0.001$) between samples. This analysis indicates that the abundance of U-rich particles has increased following AMF colonisation, with a greater quantity of U-rich particles having precipitated in the epidermis, cortex and endodermis root cell layers.

U-rich (as determined by EDS point spectra S1, S3 and ESI Fig. S2†) and another absent of U that is most likely an Al and Fe rich soil particle (as determined by EDS point spectra S2 and S4; ESI Fig. S2†).

Root U particles contain P and co-localise with Ca

SEM-EDS mapping further confirmed the presence of U-rich particles alongside a correlation between the location of U, P and oxygen (O) for both AMF and non-colonised treatments

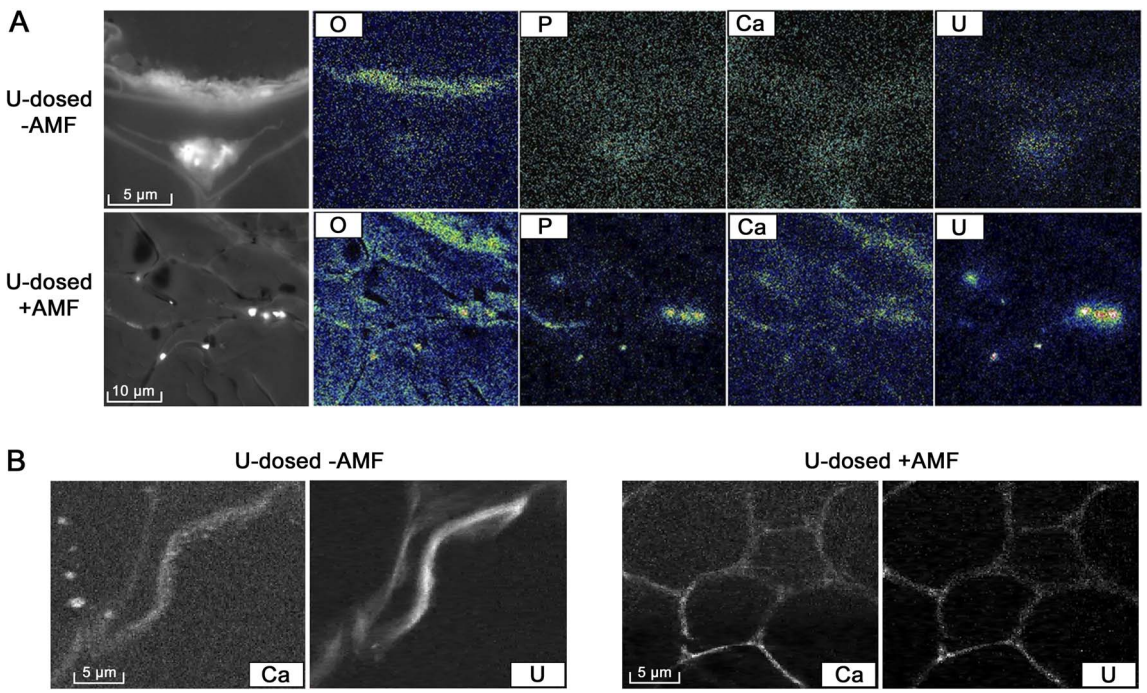

Fig. 3 SEM-EDS and SR µ-XRF imaging of U-dosed roots. (A) BSE high magnification images of selected U-dosed non-mycorrhizal (−AMF) and mycorrhizal (+AMF) root epidermal cell regions containing U-rich particles, and corresponding EDS element maps of the same regions for O, P, Ca, and U. Images are representative of multiple thin sections and viewpoints for each section. Colour concentration scale: red = high concentration, blue/black = low concentration. The BSE images are the same mapped regions as shown in ESI Fig. S2 and S3.† (B) SR µ-XRF images showing Ca and U distribution in selected epidermal cells from representative transverse root sections of U-dosed non-mycorrhizal and AMF-colonised seedlings. Brighter regions represent a greater concentration of the target element. Scanned regions were 25 µm × 25 µm at 100 nm per pixel resolution. This figure demonstrates the co-localisation of U, P and Ca, potentially indicating the presence of a uranyl phosphate phase such as autunite ($Ca(UO_2)_2(PO_4)_2$).

(Fig. 3A). This could be indicative of uranyl phosphate phases (*e.g.*, torbernite or autunite) precipitating within the root cells. A correlation between U and Ca distribution was observed by using SEM-EDS (Fig. 3A) and SR μ-XRF (Fig. 3B) in both sets of roots, but predominantly in mycorrhizal specimens, and notably in regions adjacent to root cell walls. Control (un-dosed) samples were also analysed by SR μ-XRF to demonstrate that the U signal was absent, and to examine baseline elemental distribution (*e.g.*, for P, Fe, Zn and Cu) within epidermal and cortex cells prior to dosing with uranyl(VI) showing P, Zn and Cu associated with the cell walls (ESI Fig. S6†).

To corroborate the results acquired from the X-ray techniques and generate images with high sensitivity and subcellular detail, NanoSIMS was used to identify the localisation and associations between different selected elements within root thin sections. Since natural U is comprised of 99.3% ^{238}U, this isotope of U was examined by NanoSIMS as this technique is isotopically sensitive. Control samples of *P. lanceolata* roots were also mapped to determine baseline elemental distributions for non-mycorrhizal (ESI Fig. S7†) and mycorrhizal plants (ESI Fig. S8†). For the U-dosed samples, NanoSIMS demonstrated a higher abundance of U in AMF-colonised roots compared to non-mycorrhizal roots. Furthermore, the concentration of U was high in the outermost root cell layers including the epidermis and outer cortex (Fig. 4B) and in the inner cell layers such as the endodermis and stele (Fig. 4C), whereas in

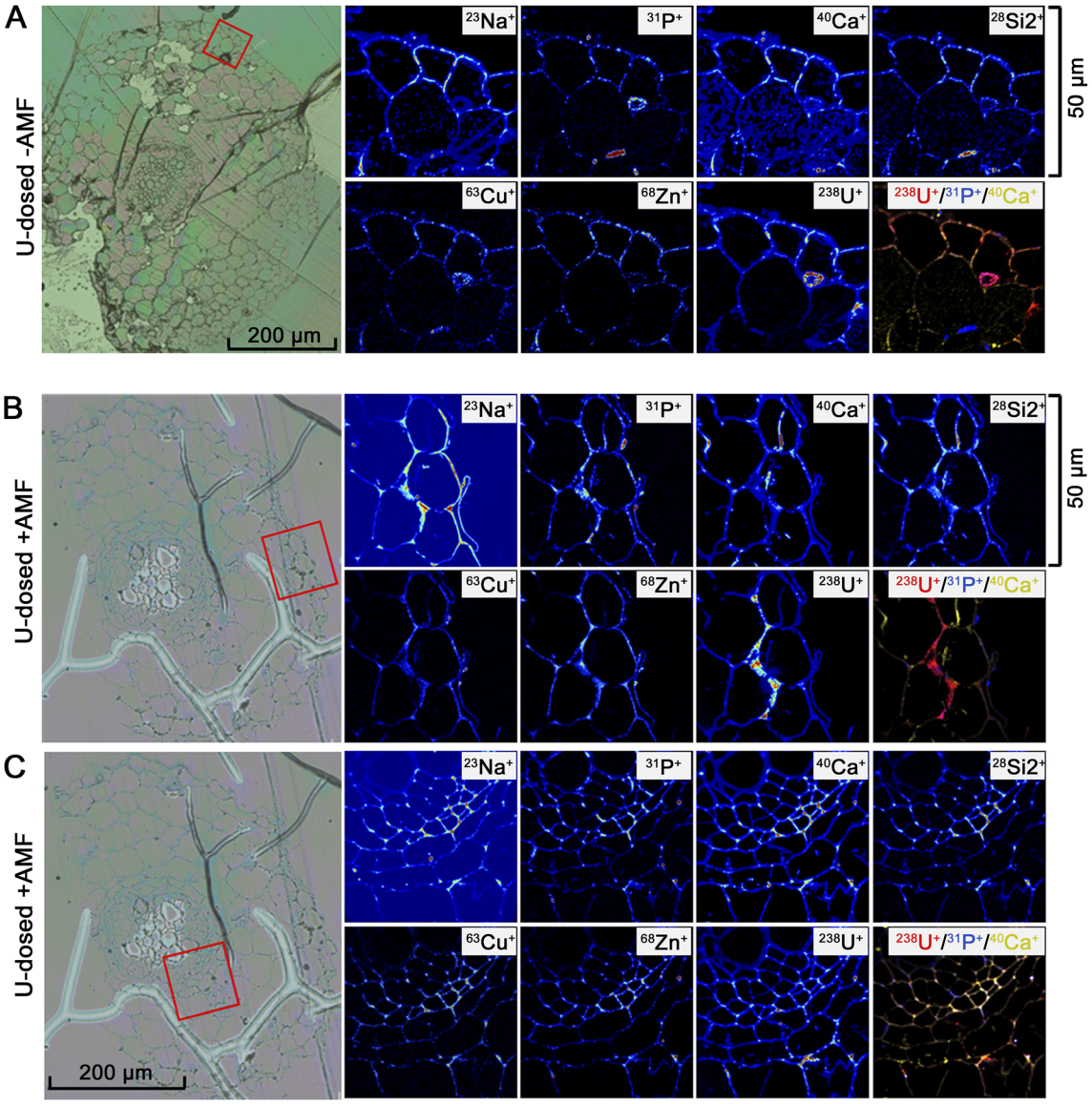

Fig. 4 NanoSIMS imaging of U-dosed roots. Optical photomicrographs of the root section (left) with NanoSIMS chemical maps (thermal colour scale) depicting elemental distributions of Na, P, Ca, Si_2, Cu, Zn and U within the epidermis of representative U-dosed, non-mycorrhizal (−AMF) root cross sections (A), and within the epidermis (B) and the endodermis/stele boundary (C) of representative U-dosed, mycorrhizal (+AMF) root cross sections. Colour merge images show the relative location of U (red), P (blue) and Ca (yellow) with whiter regions exhibiting near-equivalent concentrations of all three elements. This figure presents the co-localisation of U, P and Ca, within the epidermis and endodermis of the root sections. The distribution of these three elements indicates the presence of a mixture of U compounds.

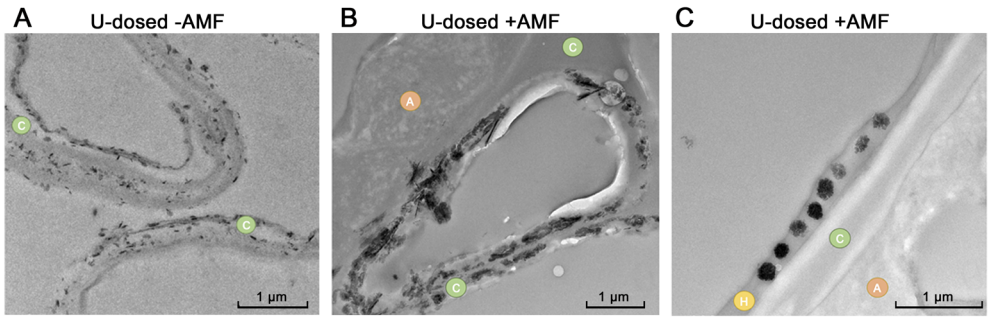

Fig. 5 TEM images of U-rich crystals in U-dosed roots. (A) Acicular U-rich crystals present within the cell walls of a representative non-mycorrhizal (−AMF), U-dosed root section. (B) Acicular U-rich crystals present within the cell walls of a representative mycorrhizal (+AMF), U-dosed root section. (C) U-rich rounded aggregates present within the fungal tissues of a representative mycorrhizal (+AMF), U-dosed root section. Plant cell walls (indicated by 'C' symbol), arbuscules (indicated by 'A' symbol) and hyphal tissue (indicated by 'H' symbol) are annotated in each image. This figure demonstrates that whilst acicular structures containing U were visible in both plant sections, irrespective of AMF colonisation, a unique rounded aggregate can be seen within only the AMF-colonised root specimens. These rounded aggregates were observed in AMF tissue cells, which were not observed in the −AMF root sections.

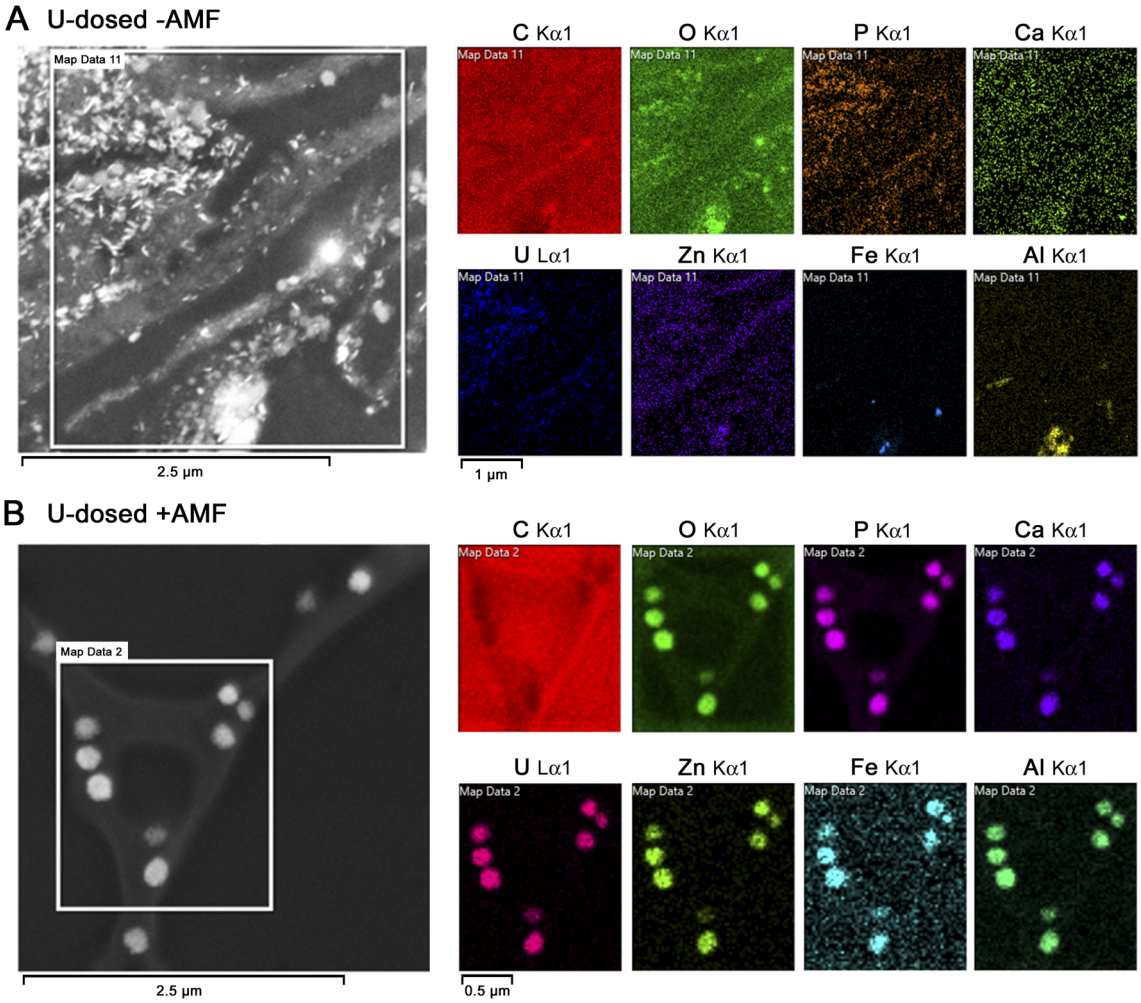

Fig. 6 BSE images of U-rich crystals in U-dosed roots. (A) U-rich acicular crystals present within the cell wall of a representative non-mycorrhizal (−AMF) root section of U-dosed seedlings. (B) U-rich rounded aggregates present within a representative mycorrhizal (+AMF) root section of U-dosed seedlings. Elemental maps generated by STEM-EDS (C, O, P, Ca, U, Zn, Fe and Al) are displayed, with brighter colouration corresponding to a greater concentration of that element. This STEM-EDS analysis supports the finding of U, P and Ca co-localisation and the presence of at least two U morphologies: the acicular needle and the rounded aggregate.

non-mycorrhizal roots U was abundant only in the outer epidermal cell walls (Fig. 4A). The greatest concentration of U was seen to reside within deposits along the walls of the outer epidermal and cortical cells. In the optical micrographs, these deposits show morphological similarity to previously observed callose deposits.[39] These deposits are more prevalent within AMF-inoculated samples, explaining the greater abundance of U particles found within the AMF-colonised plants relative to the un-colonized (Fig. 4). There was an association between U and P (represented as $^{31}P^{+}$ ions) and an intermittent association between U and Ca (represented as $^{40}Ca^{+}$ ions) for both non-mycorrhizal (Fig. 4A) and mycorrhizal plants (Fig. 4B and C). The NanoSIMS mapping data also indicates a potential relationship between U and Cu (represented as $^{63}Cu^{+}$ ions).

AMF-colonised root cells have U particles with different crystalline morphology and elemental composition

TEM imaging showed distinct morphological characteristics for the U particles within the root sections (Fig. 5). Acicular (needle-like) crystals were observed in both non-mycorrhizal (Fig. 5A) and AMF-colonised (Fig. 5B) roots of U-dosed *P. lanceolata.* However, in the AMF-colonised root sections the U particles also appeared to take the form of smaller, rounded aggregates (Fig. 5C). These rounded particles were found within the filamentous AMF fungal tissues whilst the acicular crystals were found exclusively within the cell walls of the root cells (Fig. 5; ESI Fig. S9†).

STEM-EDS, which provided better resolution within the thin sections than SEM-EDS, confirmed that the acicular and rounded particles contained U (Fig. 6; ESI Fig. S10†). STEM-EDS mapping also confirmed the association between U, P, Ca and O. Within the non-mycorrhizal samples, the presence of acicular crystals containing U, P, Ca and O were observed (Fig. 6A). Likewise, the rounded aggregates in mycorrhizal roots contained an alternative form of U that also overlapped with P and O (Fig. 6B), indicative of a uranyl phosphate compound with a unique morphology in the mycorrhizal roots. Both forms of the particles had an association between Zn and U; however, only the rounded aggregates of U particles also displayed strong association with other metals including Fe and Al (Fig. 6B), as well as with Cu (ESI Fig. S10†).

U is precipitated as a uranyl orthophosphate within root cells in the presence or absence of AMF

U speciation in *P. lanceolata* roots and shoots was determined using XANES and EXAFS analyses. Bulk XANES spectroscopy and μ-XANES mapping were used to distinguish the oxidation state of U in both the non-mycorrhizal and AMF-colonised roots and shoots. Bulk XANES spectra were acquired at the L_3 edge for plant samples and compared to two reference compounds:

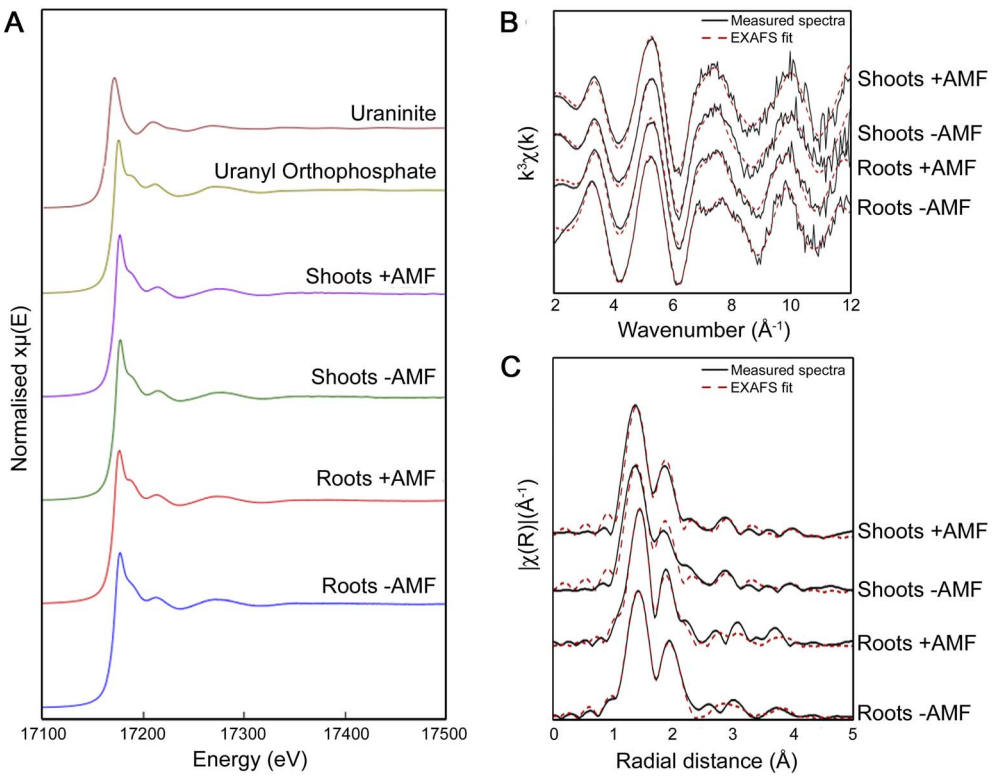

Fig. 7 (A) Bulk U L_3 edge XANES shoot and root spectra for U-dosed non-mycorrhizal (−AMF) and mycorrhizal (+AMF) specimens, and for uranyl orthophosphate (U(VI)) and uraninite (U(IV)) standards. The U(IV) edge position from uraninite occurs at 17 169 eV, and the U(VI) edge from uranyl orthophosphate occurs at 17 171 eV. (B and C) U EXAFS *k*-space spectra (B) and Fourier Transform spectra (C) acquired from L_3-edge analysis of shoot and root spectra for U-dosed non-mycorrhizal (−AMF) and mycorrhizal (+AMF) specimens. Black solid lines represent collected spectra while the red dashed line indicates the modelled best-fit spectra. This figure suggests that the dominant U oxidation state in all of the shoot and root section treatments is U(VI), akin to uranyl orthophosphate, irrespective of AMF colonisation status.

uranyl orthophosphate (U(VI)) and uraninite (U(IV)). XANES analysis indicates that the dominant U oxidation state was U(VI) in uranyl coordination within the plant roots and shoots, irrespective of AMF-colonisation status, as inferred from the edge position and overall shape of all the plant-derived spectra compared with the position, shape and maximum first derivative of the uranyl orthophosphate reference spectrum (Fig. 7A). In particular, the presence of an extended shoulder at ~17.190 keV succeeding the main peak is characteristic of the uranyl ion.[25] These XANES features were also observed during μ-XANES mapping of the *P. lanceolata* thin sections, illustrating similar spectra for known U-abundant regions within the epidermal root cell layers of the tissues, irrespective of AMF treatment (ESI Fig. S11†).

EXAFS analyses were conducted to deduce the local coordination environment (*e.g.*, main ligands present) of the uranyl structure within the plant samples. Peak distribution between all four spectra was very similar within the *k* space (Fig. 7B) and for the Fourier transform spectra (Fig. 7C) indicating that the speciation of U within the plant shoots and roots are unlikely to differ significantly, irrespective of AMF colonisation. The fit data indicate that the U(VI) is coordinated by two axial oxygens at ~1.78 Å and five equatorial oxygens at 2.30–2.49 Å. This is followed by three P shells at ~3.16, ~3.60 and ~3.70 Å. Finally, a U shell at ~4.00 Å was also indicated. The high-quality *k*-space data enables the ability to model two equatorial U scattering paths and three separate U–P bonds. Overall, the measured EXAFS spectra from the roots and shoots of the non-mycorrhizal and AMF-colonised *P. lanceolata* samples (black line) showed good agreement with the modelled fit (red dotted line) up to a wavenumber of 12 $Å^{-1}$ (Fig. 7B).

As observed from the elemental mapping and TEM morphological characterisation, there are at least two different U compounds present within the roots of the U-dosed *P. lanceolata*, each demonstrating U–P co-localisation but also with some potential U–Ca co-localisation. Uranyl orthophosphate ($(UO_2)_3(PO_4)_2 \cdot 4H_2O$) and autunite ($Ca(UO_2)_2(PO_4)_2 \cdot 6H_2O$) are two reported mineral compounds that could form within plant roots,[25] so the plant EXAFS spectra were compared against the scattering paths and distances for these two mineral compounds. Whilst the shells of atoms surrounding U(VI) in orthophosphate and autunite both occur at relatively similar distances, the presence of a U–P bond in orthophosphate at ~3.16 Å (indicative of a bidentate phosphate ligand and absent in autunite) enables uranyl orthophosphate dominance to be distinguished. The bond at ~3.16 Å corresponds to a position of ~2.35 Å in Fig. 7C, owing to known energy shift. The similarity of the root and shoot spectra to uranyl orthophosphate can also be observed in the EXAFS *k*-space and Fourier-transform spectra when compared to the uranyl orthophosphate standard, which could be fit reliably to a *k*-range of up to 16 $Å^{-1}$ (ESI Fig. S12†). However, due to the similarity in the structure of autunite and uranyl orthophosphate this EXAFS fit may also be indictive of the presence of both compounds within the roots and shoots. Furthermore, given the correlation between U, P and Ca observed in the elemental maps we suggest that both phases are likely to be present. Overall, it is apparent from the EXAFS analysis that the presence or absence of AMF within the *P. lanceolata* roots did not significantly influence the dominant U speciation.

Discussion

Plant tissue U partitioning and mycorrhizal colonisation

Root growth of the *P. lanceolata* seedlings was impaired by uranyl(VI) exposure. U growth inhibition has been well documented for many plant species and is likely to be due in part to an oxidative stress response.[24,40] Restricted root-to-shoot translocation of U, which causes increased partitioning of U within the roots, exacerbates root growth inhibition.[8,12] Approximately 1% of the total available U was accumulated by the plants, a much higher value than the typical soil-to-plant concentration ratio of 0.0045.[41] This was due to the use of a sand substrate and a highly soluble uranyl(VI) solution, intended to maximise U uptake to enable sufficient detection and analysis. As shown in prior studies, natural organic soils display more complex U speciation than will be observed in the sand matrix used within this study. Soil texture, organic matter content and redox chemistry, alongside varied geomicrobiology, will all have a significant influence on the bioavailability of U to plants. Therefore, whilst this study provides an essential mechanistic insight into the potential contribution of AMF in influencing U speciation and localisation within plant roots, absent of these confounding environmental variables, further work should be done within more environmentally-relevant systems to compare with the findings of this study.[8,9,42] With regard to U speciation within the plant, XANES U L_3 edge analysis showed that uranyl uptake resulted in the formation of U(VI) compounds within root and stem tissues, which is consistent with the findings of Laurette *et al.*,[25] indicating that U(VI) is a conserved oxidation state for bioaccumulated U.

U dosing had no consequence on root AMF colonisation, which was consistent with measurements for *R. irregularis* infected *P. lanceolata* from previous studies.[9,43] Although some prior studies have indicated that the presence of AMF may enhance U uptake into roots,[3,44] this study found insignificant differences for mean shoot and root U concentration between mycorrhizal and non-mycorrhizal plants. AMF networks can be highly efficient at enhancing the uptake of elements from soil, including non-essential elements that have chemical similarity to essential micronutrients.[3,45] One explanation for the lack of difference in plant U accumulation following AMF treatment (alongside P and other nutrients) in this study is that the highly bioavailable conditions provided by the sand and the provision of a plentiful nutrient solution negated any benefits from the presence of a hyphal network, reducing the reliance on the plant to utilise the AMF for acquiring additional nutrients like P (and potentially U and other trace metals concurrently). This is supported by prior studies that have observed reduced AMF colonisation in high P environments, which in turn may limit hyphal network production.[46,47] Whilst the results of this study imply that AMF is of limited use for phytoextraction of U from contaminated environments, it is still possible that AMF may be influential in controlling soil conditions (*e.g.*, alteration of pH

via secretion of organic acids)[48] to enhance U mineral solubility and bioavailability for accumulation into plant and fungal tissues. This may also reduce the bioavailability of U once within the root, which would have consequences for the success of phytostabilization strategies.[49] It is also theorised that AMF-associated phytoremediation strategies will be valuable for decontamination of sites comprising sandy or dry soil. Under these conditions, the secretion of glycoproteins by AMF (*e.g.*, glomalin-related soil proteins) may help bind soil aggregates together and sorb heavy metals, minimising migration of U-contaminated particles, whilst using the mycelial network to acquire supplementary U from soil *in lieu* of the high cation exchange capacity of clay and organic-rich soils.[50] Furthermore, the success of these phytoremediation strategies may also be dependent on the abiotic conditions of the soil environment and on the specific host plant and AMF species partnership that is being utilised.

Elemental mapping and U speciation

U-rich particles were located along plant cell walls and membranes, rather than within the vacuole or other organelles, in both the non-mycorrhizal and AMF-colonised plants. This was consistent with previous studies showing U precipitates along the root cell walls of various plant species.[23,24] In this study, it was also apparent that U-rich regions were widely located within epidermal root cells of both non-mycorrhizal and mycorrhizal samples, where cell wall binding or formation of precipitates potentially limited the ability for U transfer to the xylem. In mycorrhizal roots, U-rich particles were also predominant within fungal hyphal tissues. NanoSIMS analysis indicated that the distribution of U within the epidermal cell layer is coincident with the presence of thickened deposits seen by optical microscopy, which are likely to be callose deposits, although this could not be definitively confirmed here. Callose deposition within epidermal cell layers is a common response to microbial pathogens[51] or metal stress,[52] and also characteristic of AMF colonisation.[53,54] Some of the epidermal cells for the U dosed plants were more irregular in shape compared to undosed samples, which could be a result of developmental stress from excess U absorption during seedling growth.[24]

The SEM- and STEM-EDS results showed a correlation between U, P and O distribution within root cells, as also seen in other plant species.[17,19,23] This suggests that once U is absorbed into the roots and fungal tissues from the surrounding substrate, it is immobilised and precipitated as uranyl phosphate biominerals, which have a relatively low solubility under neutral pH conditions relative to other U phases.[55] This immobilisation of U would be beneficial for the AMF and its plant host, limiting the migration and accessibility of U to the xylem within the stele layer of the roots, and thus restricting root-shoot transfer and toxic exposure. EXAFS analysis modelled the axial ($U–O_{ax}$), equatorial ($U–O_{eq}$) and phosphate (U–P) bonds, similar to the process followed by Laurette *et al.*,[25] and confirmed uranyl orthophosphate to be the dominant U compound in the *P. lanceolata* tissues, but irrespective of AMF treatment. This aligns with the conserved presence of the acicular U crystals, which are proposed to be predominantly uranyl orthophosphate, and aligns with the results of Fomina *et al.*,[56] who observed that thermodynamically stable uranyl phosphate minerals are the primary U biomineralisation product.

A correlation between U- and Ca-rich regions was also demonstrated by elemental mapping and SR μ-XRF. SR μ-XRF was an effective high-resolution and high sensitivity method to validate U distribution and the co-location of U–Ca at plant cell walls.[22] But SR μ-XRF was less suitable to confirm U–P co-localisation as the use of hard X-rays is less effective at mapping lighter elements like P. In contrast, NanoSIMS, which has previously been used to study multiple element interactions in plants,[17,57–59] successfully validated the co-localisation of U with P and Ca, as well as other metals including Cu and Zn within the root cells. The correlations between U and Ca, and U and Cu, suggests the presence in some cells of autunite and torbernite, respectively. EXAFS analysis indicated the potential for autunite as well as uranyl orthophosphate to be present within the roots. However, EXAFS cannot easily differentiate the identity of U compounds with very similar structural chemistry, such as *meta*-autunite ($Ca(UO_2)_2(PO_4)_2$ $6(H_2O)$) and *meta*-torbernite ($Cu(UO_2)_2(PO_4)_2$ $8(H_2O)$).[60]

Previous studies have also observed a relationship between U, P and Ca,[17,61] with suggestions that the presence of U may inhibit cell growth due to reduced availability of inorganic phosphate for use in essential metabolic processes, and that Ca content may govern the mobility of U and its accessibility to the xylem. However, the influence of AMF directly on the formation of U, P and Ca rich deposits had not been previously examined. Chen *et al.*[19] suggested that increased root partitioning of U in barley following inoculation with an AMF species was due to enhanced complexation with P, although no elemental mapping evidence was provided. There was also evidence in this current study of a correlation between U and Zn. Both elements form divalent cations in solution and undergo similar chemical bonding reactions to organic and inorganic ligands, including to phosphate, which may result in co-localisation within plant root cells.

U crystal morphology

Biomineralisation is a conserved process in plants and fungi, and it is thought to be important in controlling free metal ion concentrations within cells and preventing toxicity of metals.[62,63] Likewise, it is proposed that the U and trace metal containing biominerals observed here are also providing a detoxification role. The formation of two distinct morphologies of crystalline U biominerals within the plant root cells, with one morphology being solely present within the AMF-colonised roots, is intriguing and to our knowledge, has not been previously reported in the literature. Acicular U-rich particles have previously been observed within the root cell walls of *A. thaliana*[17] and at root cell walls in sunflower and oilseed rape.[23] However, these studies did not observe the rounded aggregate U-rich morphology. Cell wall associated U- and P-rich precipitates on hyphae of ericoid and

ectomycorrhizal fungi have previously been characterised, but these U precipitates formed on external hyphal surfaces and outside of plant tissues.[26,56] Misson *et al.*[17] proposed that uranyl phosphate deposits may demonstrate different morphologies depending on their location within the root cells, and referred to a U, P and Ca rich granular structure within the cytoplasm. Although, the exact morphology of these granules was poorly resolved, they were different to the rounded nanoscale aggregate structures observed here. One possibility is that the rounded aggregate form of U observed in hyphal tissues within the root cells may be a U-phosphate phase, such as autunite or torbernite,[64] which would align with prior published studies.[65] In contrast, a logical option for the acicular form would be uranyl orthophosphate, which has previously been found to form needle-like crystals when synthesised.[66] There is also the possibility that the nanoparticle needles are the progeny of tetrahedral or trigonal crystal habits of phosphuranylite.[65,67]

It is unclear why two different U compounds, each comprising similar base constituents of U, P and Ca, would form within the root cells following mycorrhizal colonisation. One possible cause is that the AMF will secrete organic acids (*e.g.*, citric and oxalic acids) and acid phosphatase enzymes from the intracellular hyphae that will separate inorganic phosphate ions from metal complexes, such as within U-phosphate minerals. These metals will then precipitate into new secondary phases such as U-carboxylates, U-citrates and U-oxalates.[48,64] An influx of phosphate ions into the intracellular hyphae may result in enhanced complexation with soluble U species (*e.g.*, UO_2^{2+}) to form *in situ* insoluble U-phosphate minerals.[27] It is also possible that glomalin present in the hyphae may be responsible for enhancing metal sorption and complexation within the fungal tissues,[68] although the precise involvement of glomalin-like proteins in mediating metal binding is poorly understood. Multiple prior studies have shown that for other free-living and ectomycorrhizal fungi, secondary U biomineralisation through the interaction of U (derived from U-hydroxide complexes) and inorganic phosphate generated a myriad of U phosphate minerals beyond *meta*-autunite; including uramphite ($NH_4UO_2PO_4 \cdot 3H_2O$), chernikovite ($(H_3O)_2(UO_2)_2(PO_4)_2 \cdot 6H_2O$) and *meta*-ankoleite ($K(UO_2)(PO_4) \cdot 3H_2O$).[26,27] These studies with free-living fungi have shown that this precipitation is mycogenic in nature, such as in the formation of U-rich aggregates formed by *Aspergillus niger* when exposed to soluble U and P.[27] Furthermore, it was observed in these studies that the formed U minerals were localised and crystallised along the hyphal tissues of these fungal agents, akin to the rounded aggregates observed within this study. It is likely that a similar biomineralisation process is occurring within the intracellular hyphae of the AMF. The similar elemental components and chemical structure of these U phosphate minerals may limit the accuracy of EXAFS analysis for confirming the exact contributing U phosphate minerals within the intracellular AMF hyphal network, though it is plausible that a mixture of all of these U phases is present to varying extents.

It is clear that the hyphal-localised rounded aggregate U particles associated with metals including Fe and Cu, which was not the case for the cell wall localised acicular U particles. This may potentially be to reduce U toxicity or to more effectively limit mobility of excess U. Analogous to this, Li *et al.*[69] described variation in cadmium (Cd) precipitation between AMF-colonised and non-mycorrhizal rice plants whereby the roots of mycorrhizal plants had more phosphate- or pectate-bound forms of Cd compared to non-mycorrhizal plants, suggesting that the AMF was facilitating the transformation of Cd into less mobile and less toxic forms. However, it is not currently possible to confirm that the sole cause for the occurrence of the rounded aggregate U form is due to the presence of AMF, nor is it possible to determine the role of AMF in altering U morphology. It is also possible that the rounded aggregates may be specific to *R. irregularis*, with different U morphologies forming within other AMF species.

Another possible reason for the presence of both uranyl orthophosphate and autunite relates to the pathway of U phosphate crystallisation. It has been observed experimentally that uranyl orthophosphate is often the first U(VI) phosphate to precipitate from an oversaturated solution, which will then crystallise to more thermodynamically stable phases over time (*e.g.*, autunite). Therefore, the presence of both phases within plant tissues may represent the time since U phosphate precipitation, with recently precipitated particles still present as uranyl orthophosphate, whilst aged particles have formed autunite.[70] Furthermore, it is realistic to expect that alongside uranyl orthophosphate and autunite, there are smaller proportions of other U species such as U-citrates, U-carboxylates and other U-phosphate minerals (*e.g.* uramphite, chernikovite),[64] as seen in previously published studies associated with plant-U uptake and U biomineralisation by fungi.[26,27] Future work should better confirm the chemical identity of the acicular and aggregate structures, potentially with a targeted μ-XANES mapping study of each crystal structure, as well as determining the possible functional relevance. Additional studies could also determine whether this dual morphology is observed within different plant host and AMF species associations. Nonetheless, these findings provide new understanding of the potential mechanism for how AMF colonisation may alter U storage and transfer processes in plants, such as biomineralisation to reduce toxicity and restrict transfer into other parts of the plant.

Conclusions

This investigation has provided a novel insight into how AMF influences U uptake and storage in *P. lanceolata* roots, in particular through the discovery of a previously unreported rounded aggregate nanoparticle forming in the fungal tissues. Through elemental mapping, it was confirmed that U-rich particles preferentially form on the cell walls of the root cells, and there was a direct correlation between U, P, Ca and O, indicating that U is likely being transformed into a uranyl phosphate solid. Only an acicular form of U phosphate was present within non-mycorrhizal samples whilst AMF-colonised roots displayed both an acicular form and the distinct rounded aggregate form that appears to localise in fungal cells embedded within the plant cells. A correlation between U and

Ca could suggest that autunite may be a component of the aggregate structure, whilst the acicular particles are a variant of uranyl orthophosphate. The formation of these different crystalline U precipitates is likely due to differences in crystallisation time and intracellular metal availability in the plant and fungal cells. XANES analysis confirmed that the major oxidation state for U within the roots was U(VI) irrespective of AMF treatment. Although it is likely that both a uranyl orthophosphate and an autunite or *meta*-autunite mineral form are being precipitated within tissues, the uranyl orthophosphate form dominates according to EXAFS modelling, and might provide a means to limit the mobility and phytotoxicity of U. It is likely that alongside uranyl orthophosphate and autunite, biogenic contributions of U *via* U-citrate, U-oxalate and U-carboxylate complexes alongside alternative secondary U phosphate minerals (*e.g.*, uramphite, chernikovite and *meta*-ankoleite) could be expected, as has been observed for previous studies examining U biomineralisation for alternative fungal groups and plant species. This biomineralisation process could be exploited to transform mobile U(VI) with soils into an insoluble form, reducing the toxicity of the U(VI) present and potentially acting as a mechanism of U phytoremediation. As plant U uptake was insignificantly affected by AMF colonisation, yet the storage of U differed through the presence or absence of the rounded U-rich aggregates, it is possible that organic acids produced by the AMF will influence U speciation both *in planta* (intracellular hyphae) and within the soil (*via* the external mycelial network), potentially resulting in AMF being more valuable for phytostabilisation than phytoextraction of U-contaminated sites.

Future work must examine if this U storage behaviour is observed within other AMF-plant host partnerships, and within more environmentally relevant soil conditions, in order to determine the applicability of these findings for optimising ecosystem transfer models for U. This might involve examining native AMF-plant species partnerships under varying geophysical and geochemical conditions across known U-contaminated sites to establish differences in U absorption and particle morphology within the native plant and AMF tissues, utilising the same analytical techniques within this study. By conducting high-resolution, mechanistic studies and field-relevant investigations, a more detailed understanding of the role of AMF in influencing U speciation, transfer and storage in plants and soil can be obtained.

Data availability

The data supporting this article have been included as part of the ESI.†

Author contributions

James Dinsley: conceptualization, data curation, formal analysis, funding acquisition, investigation, methodology, validation, visualization, writing – original draft, writing – review & editing. Kirstie Halsey: investigation, methodology. Eudri Venter: data curation, investigation, methodology. Miguel Gomez-Gonzalez: data curation, formal analysis, investigation, supervision. Katie Moore: data curation, formal analysis, funding acquisition, investigation, methodology, supervision, writing – review & editing. Lorraine Field: data curation, formal analysis, investigation, supervision, writing – review & editing. Samuel Shaw: conceptualization, formal analysis, supervision, writing – review & editing. Clare Robinson: conceptualization, supervision, writing – review & editing. Jon Pittman: conceptualization, formal analysis, funding acquisition, project administration, supervision, writing – original draft, writing – review & editing.

Conflicts of interest

There are no conflicts to declare.

Acknowledgements

This project was supported by a Natural Environmental Research Council (NERC) PhD studentship (grant no. NE/L002469/1) and a British Geological Survey British Universities Funding Initiative (BUFI) research grant (grant no. GA/18S/027/A1). The NanoSIMS work was funded by UK Research Partnership Investment Funding (UKRPIF) Manchester RPIF Round 2 and supported by the Henry Royce Institute for Advanced Materials, funded through EPSRC grants EP/R00661X/1, EP/S019367/1, EP/P025021/1 and EP/P025498/1. We acknowledge access to the NNUF RADER Facility funded through grant EP/T011300/1. The Diamond Light Source is acknowledged for beamtime on the I14 beamline (MG25930-3), B18 beamline (SP24074-8) and I20 beamline (SP21441-11). We thank staff in the Manchester Geochemical Unit (Department of Earth and Environmental Sciences, The University of Manchester) and British Geological Survey for performing ICP-MS analysis. We also thank Kath Morris and Giannantonio Cibin for assistance with B18 beamline time, Fred Mosselmans for I20 beamline assistance and sample analysis guidance, Olwen Stagg, Callum Robinson and Luke Townsend for assisting with XAS data analysis, and Helena Davies for performing preliminary experiments.

References

1 N. Mitchell, D. Perez-Sanchez and M. C. Thorne, A review of the behaviour of U-238 series radionuclides in soils and plants, *J. Radiol. Prot.*, 2013, **33**, R17–R48.
2 C. Degueldre and M. J. Joyce, Evidence and uncertainty for uranium and thorium abundance: A review, *Prog. Nucl. Energy*, 2020, **124**, 103299.
3 J. Rosas-Moreno, C. Walker, K. Duffy, C. Krüger, M. Krüger, C. H. Robinson and J. K. Pittman, Isolation and identification of arbuscular mycorrhizal fungi from an abandoned uranium mine and their role in soil-to-plant transfer of radionuclides and metals, *Sci. Total Environ.*, 2023, **876**, 162781.
4 P. J. C. Favas, J. Pratas, S. Mitra, S. K. Sarkar and P. Venkatachalam, Biogeochemistry of uranium in the soil-

plant and water-plant systems in an old uranium mine, *Sci. Total Environ.*, 2016, **568**, 350–368.
5 P. Zhou and B. Gu, Extraction of oxidized and reduced forms of uranium from contaminated soils: effects of carbonate concentration and pH, *Environ. Sci. Technol.*, 2005, **39**, 4435–4440.
6 G. T. W. Law, A. Geissler, I. T. Burke, F. R. Livens, J. R. Lloyd, J. M. McBeth and K. Morris, Uranium redox cycling in sediment and biomineral systems, *Geomicrobiol. J.*, 2011, **28**, 497–506.
7 L. Newsome, K. Morris, D. Trivedi, N. Atherton and J. R. Lloyd, Microbial reduction of uranium(VI) in sediments of different lithologies collected from Sellafield, *Appl. Geochem.*, 2014, **51**, 55–64.
8 H. S. Davies, J. Rosas-Moreno, F. Cox, P. Lythgoe, A. Bewsher, F. R. Livens, C. H. Robinson and J. K. Pittman, Multiple environmental factors influence ^{238}U, ^{232}Th and ^{226}Ra bioaccumulation in arbuscular mycorrhizal-associated plants, *Sci. Total Environ.*, 2018, **640–641**, 921–934.
9 J. Rosas-Moreno, J. K. Pittman and C. H. Robinson, Specific arbuscular mycorrhizal fungal–plant interactions determine radionuclide and metal transfer into *Plantago lanceolata*, *People Planet*, 2021, **3**, 667–678.
10 H. B. L. Pettersson, G. Hancock, A. Johnston and A. S. Murray, Uptake of uranium and thorium series radionuclides by the waterlily, *Nymphaea violacea*, *J. Environ. Radioact.*, 1993, **19**, 85–108.
11 S. Yoshida, Y. Muramatsu, K. Tagami, S. Uchida, T. Ban-nai, H. Yonehara and S. Sahoo, Concentrations of uranium and ^{235}U/^{238}U ratios in soil and plant samples collected around the uranium conversion building in the JCO campus, *J. Environ. Radioact.*, 2000, **50**, 161–172.
12 P. Soudek, Š. Petrová, D. Benešová, M. Dvořáková and T. Vaněk, Uranium uptake by hydroponically cultivated crop plants, *J. Environ. Radioact.*, 2011, **102**, 598–604.
13 L. Duquène, H. Vandenhove, F. Tack, E. Van der Avoort, M. Van Hees and J. Wannijn, Plant-induced changes in soil chemistry do not explain differences in uranium transfer, *J. Environ. Radioact.*, 2006, **90**, 1–14.
14 R. Wetle, B. Bensko-Tarsitano, K. Johnson, K. G. Sweat and T. Cahill, Uptake of uranium into desert plants in an abandoned uranium mine and its implications for phytostabilization strategies, *J. Environ. Radioact.*, 2020, **220–221**, 106293.
15 M. D. Stojanović, M. L. Mihajlović, J. V. Milojković, Z. R. Lopičić, M. Adamović and S. Stanković, Efficient phytoremediation of uranium mine tailings by tobacco, *Environ. Chem. Lett.*, 2012, **10**, 377–381.
16 N. B. C. Serre, C. Alban, J. Bourguignon and S. Ravanel, Uncovering the physiological and cellular effects of uranium on the root system of *Arabidopsis thaliana*, *Environ. Exp. Bot.*, 2019, **157**, 121–130.
17 J. Misson, P. Henner, M. Morello, M. Floriani, T.-D. Wu, J.-L. Guerquin-Kern and L. Février, Use of phosphate to avoid uranium toxicity in *Arabidopsis thaliana* leads to alterations of morphological and physiological responses regulated by phosphate availability, *Environ. Exp. Bot.*, 2009, **67**, 353–362.
18 H.-H. Zhang, M. Tang, H. Chen, C.-L. Zheng and Z.-C. Niu, Effect of inoculation with AM fungi on lead uptake, translocation and stress alleviation of *Zea mays* L. seedlings planting in soil with increasing lead concentrations, *Eur. J. Soil Biol.*, 2010, **46**, 306–311.
19 B. Chen, Y.-G. Zhu, X. Zhang and I. Jakobsen, The influence of mycorrhiza on uranium and phosphorus uptake by barley plants from a field-contaminated soil, *Environ. Sci. Pollut. Res.*, 2005, **12**, 325–331.
20 G. Rufyikiri, Y. Thiry and S. Declerck, Contribution of hyphae and roots to uranium uptake and translocation by arbuscular mycorrhizal carrot roots under root-organ culture conditions, *New Phytol.*, 2003, **158**, 391–399.
21 B. D. Chen, Y. G. Zhu and F. A. Smith, Effects of arbuscular mycorrhizal inoculation on uranium and arsenic accumulation by Chinese brake fern (*Pteris vittata* L.) from a uranium mining-impacted soil, *Chemosphere*, 2006, **62**, 1464–1473.
22 J. M. Dinsley, H. S. Davies, M. A. Gomez-Gonzalez, C. H. Robinson and J. K. Pittman, The value of synchrotron radiation X-ray techniques to explore microscale chemistry for ecology and evolution research, *Ecosphere*, 2022, **13**, e4312.
23 J. Laurette, C. Larue, C. Mariet, F. Brisset, H. Khodja, J. Bourguignon and M. Carriere, Influence of uranium speciation on its accumulation and translocation in three plant species: Oilseed rape, sunflower and wheat, *Environ. Exp. Bot.*, 2012, **77**, 96–107.
24 J.-l. Lai, Z.-w. Liu, C. Li and X.-g. Luo, Analysis of accumulation and phytotoxicity mechanism of uranium and cadmium in two sweet potato cultivars, *J. Hazard. Mater.*, 2021, **409**, 124997.
25 J. Laurette, C. Larue, I. Llorens, D. Jaillard, P.-H. Jouneau, J. Bourguignon and M. Carrière, Speciation of uranium in plants upon root accumulation and root-to-shoot translocation: A XAS and TEM study, *Environ. Exp. Bot.*, 2012, **77**, 87–95.
26 M. Fomina, J. M. Charnock, S. Hillier, R. Alvarez and G. M. Gadd, Fungal transformations of uranium oxides, *Environ. Microbiol.*, 2007, **9**, 1696–1710.
27 X. Liang, S. Hillier, H. Pendlowski, N. Gray, A. Ceci and G. M. Gadd, Uranium phosphate biomineralization by fungi, *Environ. Microbiol.*, 2015, **17**, 2064–2075.
28 I. Skrynetska, J. Karcz, G. Barczyk, M. Kandziora-Ciupa, R. Ciepał and A. Nadgórska-Socha, Using *Plantago major* and *Plantago lanceolata* in environmental pollution research in an urban area of Southern Poland, *Environ. Sci. Pollut. Res.*, 2019, **26**, 23359–23371.
29 K. L. Moore, E. Lombi, F.-J. Zhao and C. R. M. Grovenor, Elemental imaging at the nanoscale: NanoSIMS and complementary techniques for element localisation in plants, *Anal. Bioanal. Chem.*, 2012, **402**, 3263–3273.
30 S. E. Smith and D. Read, *Mycorrhizal Symbiosis*, Academic Press, London, 3rd edn, 2008.

31 D. Thiem, A. Szmidt-Jaworska, C. Baum, K. Muders, K. Niedojadło and K. Hrynkiewicz, Interactive physiological response of potato (*Solanum tuberosum* L.) plants to fungal colonization and Potato virus Y (PVY) infection, *Acta Mycol.*, 2014, **49**, 291–303.

32 C. Cordier, M. J. Pozo, J. M. Barea, S. Gianinazzi and V. Gianinazzi-Pearson, Cell defense responses associated with localized and systemic resistance to *Phytophthora parasitica* induced in tomato by an arbuscular mycorrhizal fungus, *Mol. Plant-Microbe Interact.*, 1998, **11**, 1017–1028.

33 P. D. Quinn, L. Alianelli, M. Gomez-Gonzalez, D. Mahoney, F. Cacho-Nerin, A. Peach and J. E. Parker, The Hard X-ray nanoprobe beamline at Diamond Light Source, *J. Synchrotron Radiat.*, 2021, **28**, 1006–1013.

34 A. P. Morrell, H. Floyd, J. F. W. Mosselmans, L. M. Grover, H. Castillo-Michel, E. T. Davis, J. E. Parker, R. A. Martin and O. Addison, Improving our understanding of metal implant failures: Multiscale chemical imaging of exogenous metals in ex-vivo biological tissues, *Acta Biomater.*, 2019, **98**, 284–293.

35 A. J. Dent, G. Cibin, S. Ramos, A. D. Smith, S. M. Scott, L. Varandas, M. R. Pearson, N. A. Krumpa, C. P. Jones and P. E. Robbins, B18: A core XAS spectroscopy beamline for Diamond, *J. Phys.: Conf. Ser.*, 2009, **190**, 012039.

36 S. Diaz-Moreno, S. Hayama, M. Amboage, A. Freeman, J. Sutter and G. Duller, I20; the Versatile X-ray Absorption spectroscopy beamline at Diamond Light Source, *J. Phys.: Conf. Ser.*, 2009, **190**, 012038.

37 C. Foster, S. Shaw, T. S. Neill, N. Bryan, N. Sherriff, L. S. Natrajan, H. Wilson, L. Lopez-Odriozola, B. Rigby, S. J. Haigh, Y.-C. Zou, R. Harrison and K. Morris, Hydrotalcite colloidal stability and interactions with uranium(VI) at neutral to alkaline pH, *Langmuir*, 2022, **38**, 2576–2589.

38 Y. Kobae, Dynamic phosphate uptake in arbuscular mycorrhizal roots under field conditions, *Front. Environ. Sci.*, 2019, **6**, 159.

39 B. Piršelová, V. Mistríková, J. Libantová, J. Moravčíková and I. Matušíková, Study on metal-triggered callose deposition in roots of maize and soybean, *Biologia*, 2012, **67**, 698–705.

40 D. Aydin, E. Yalçin and K. Çavuşoğlu, Metal chelating and anti-radical activity of *Salvia officinalis* in the ameliorative effects against uranium toxicity, *Sci. Rep.*, 2022, **12**, 15845.

41 S. C. Sheppard, M. I. Sheppard, M.-O. Gallerand and B. Sanipelli, Derivation of ecotoxicity thresholds for uranium, *J. Environ. Radioact.*, 2005, **79**, 55–83.

42 A. J. Fuller, P. Leary, N. D. Gray, H. S. Davies, J. F. W. Mosselmans, F. Cox, C. H. Robinson, J. K. Pittman, C. M. McCann, M. Muir, M. C. Graham, S. Utsunomiya, W. R. Bower, K. Morris, S. Shaw, P. Bots, F. R. Livens and G. T. W. Law, Organic complexation of U(VI) in reducing soils at a natural analogue site: Implications for uranium transport, *Chemosphere*, 2020, **254**, 126859.

43 G. B. De Deyn, A. Biere, W. H. van der Putten, R. Wagenaar and J. N. Klironomos, Chemical defense, mycorrhizal colonization and growth responses in *Plantago lanceolata* L, *Oecologia*, 2009, **160**, 433–442.

44 C.-G. Ren, C.-C. Kong, S.-X. Wang and Z.-H. Xie, Enhanced phytoremediation of uranium-contaminated soils by arbuscular mycorrhiza and rhizobium, *Chemosphere*, 2019, **217**, 773–779.

45 C. Takenaka, A. Fukushi and Y. Matsuda, Arbuscular mycorrhizal fungi facilitate the uptake of radiocesium by *Eleutherococcus sciadophylloides* (Araliaceae) – a pot-scale and field survey, *J. For. Res.*, 2021, **26**, 101–109.

46 T. R. Cavagnaro, F. A. Smith, S. E. Smith and I. Jakobsen, Functional diversity in arbuscular mycorrhizas: exploitation of soil patches with different phosphate enrichment differs among fungal species, *Plant, Cell Environ.*, 2005, **28**, 642–650.

47 C. D. Collins and B. L. Foster, Community-level consequences of mycorrhizae depend on phosphorus availability, *Ecology*, 2009, **90**, 2567–2576.

48 A. Andrino, G. Guggenberger, S. Kernchen, R. Mikutta, L. Sauheitl and J. Boy, Production of organic acids by arbuscular mycorrhizal fungi and their contribution in the mobilization of phosphorus bound to iron oxides, *Front. Plant Sci.*, 2021, **12**, 661842.

49 P. Roos and I. Jakobsen, Arbuscular mycorrhiza reduces phytoextraction of uranium, thorium and other elements from phosphate rock, *J. Environ. Radioact.*, 2008, **99**, 811–819.

50 N. Gujre, R. Agnihotri, L. Rangan, M. P. Sharma and S. Mitra, Deciphering the dynamics of glomalin and heavy metals in soils contaminated with hazardous municipal solid wastes, *J. Hazard. Mater.*, 2021, **416**, 125869.

51 D. Ellinger, M. Naumann, C. Falter, C. Zwikowics, T. Jamrow, C. Manisseri, S. C. Somerville and C. A. Voigt, Elevated early callose deposition results in complete penetration resistance to powdery mildew in Arabidopsis, *Plant Physiol.*, 2013, **161**, 1433–1444.

52 A. Stass, Y. Wang, D. Eticha and W. Horst, Aluminium rhizotoxicity in maize grown in solutions with Al^{3+} or $Al(OH)_4^-$as predominant solution Al species, *J. Exp. Bot.*, 2006, **57**, 4033–4042.

53 D. Berdeni, T. E. A. Cotton, T. J. Daniell, M. I. Bidartondo, D. D. Cameron and K. L. Evans, The effects of arbuscular mycorrhizal fungal colonisation on nutrient status, growth, productivity, and canker resistance of apple (*Malus pumila*), *Front. Microbiol.*, 2018, **9**, 1461.

54 N. Sanmartín, V. Pastor, J. Pastor-Fernández, V. Flors, M. J. Pozo and P. Sánchez-Bel, Role and mechanisms of callose priming in mycorrhiza-induced resistance, *J. Exp. Bot.*, 2020, **71**, 2769–2781.

55 D. Gorman-Lewis, P. C. Burns and J. B. Fein, Review of uranyl mineral solubility measurements, *J. Chem. Thermodyn.*, 2008, **40**, 335–352.

56 M. Fomina, J. M. Charnock, S. Hillier, R. Alvarez, F. Livens and G. M. Gadd, Role of fungi in the biogeochemical fate of depleted uranium, *Curr. Biol.*, 2008, **18**, R375–R377.

57 K. L. Moore, M. Schröder, E. Lombi, F.-J. Zhao, S. P. McGrath, M. J. Hawkesford, P. R. Shewry and C. R. M. Grovenor, NanoSIMS analysis of arsenic and selenium in cereal grain, *New Phytol.*, 2010, **185**, 434–445.

58 K. L. Moore, Y. Chen, A. M. L. van de Meene, L. Hughes, W. Liu, T. Geraki, F. Mosselmans, S. P. McGrath, C. Grovenor and F.-J. Zhao, Combined NanoSIMS and synchrotron X-ray fluorescence reveal distinct cellular and subcellular distribution patterns of trace elements in rice tissues, *New Phytol.*, 2014, **201**, 104–115.

59 G. Ondrasek, Z. Rengel, P. L. Clode, M. R. Kilburn, P. Guagliardo and D. Romic, Zinc and cadmium mapping by NanoSIMS within the root apex after short-term exposure to metal contamination, *Ecotoxicol. Environ. Saf.*, 2019, **171**, 571–578.

60 J. G. Catalano and G. E. Brown, Analysis of uranyl-bearing phases by EXAFS spectroscopy: Interferences, multiple scattering, accuracy of structural parameters, and spectral differences, *Am. Mineral.*, 2004, **89**, 1004–1021.

61 E. El Hayek, A. J. Brearley, T. Howard, P. Hudson, C. Torres, M. N. Spilde, S. Cabaniss, A.-M. S. Ali and J. M. Cerrato, Calcium in carbonate water facilitates the transport of U(VI) in *Brassica juncea* roots and enables root-to-shoot translocation, *ACS Earth Space Chem.*, 2019, **3**, 2190–2196.

62 H. He, E. J. Veneklaas, J. Kuo and H. Lambers, Physiological and ecological significance of biomineralization in plants, *Trends Plant Sci.*, 2014, **19**, 166–174.

63 G. M. Gadd, Fungal biomineralization, *Curr. Biol.*, 2021, **31**, R1557–R1563.

64 A. Günther, G. Bernhard, G. Geipel, T. Reich, A. Roßberg and H. Nitsche, Uranium speciation in plants, *Radiochim. Acta*, 2003, **91**, 319–328.

65 J. W. Anthony, R. A. Bideaux, K. W. Bladh and M. C. Nichols, *Handbook of Mineralogy*, Mineralogical Society of America, Chantilly, VA, USA, 2001.

66 J. M. Schreyer and C. F. Baes, Jr., The solubility of uranium(VI) orthophosphates in phosphoric acid solutions, *J. Am. Chem. Soc.*, 1954, **76**, 354–357.

67 A. J. Locock and P. C. Burns, The crystal structure of triuranyl diphosphate tetrahydrate, *J. Solid State Chem.*, 2002, **163**, 275–280.

68 M. C. González-Chávez, R. Carrillo-González, S. F. Wright and K. A. Nichols, The role of glomalin, a protein produced by arbuscular mycorrhizal fungi, in sequestering potentially toxic elements, *Environ. Pollut.*, 2004, **130**, 317–323.

69 H. Li, N. Luo, L. J. Zhang, H. M. Zhao, Y. W. Li, Q. Y. Cai, M. H. Wong and C. H. Mo, Do arbuscular mycorrhizal fungi affect cadmium uptake kinetics, subcellular distribution and chemical forms in rice?, *Sci. Total Environ.*, 2016, **571**, 1183–1190.

70 V. S. Mehta, F. Maillot, Z. Wang, J. G. Catalano and D. E. Giammar, Effect of co-solutes on the products and solubility of uranium(VI) precipitated with phosphate, *Chem. Geol.*, 2014, **364**, 66–75.